Modeling of Nine-Switch-Converter Based on Virtual Leg and Its Application in DFIG Wind Generation System

Kai Wang, Jingmei Zhang, Yi Pang, Dongxing Xu, and Lei Pan

***Abstract*—This article proposes a doubly fed induction generator (DFIG) wind energy conversion system (WECS) based on nine-switch converter. In this article, a new concept of virtual-leg is proposed, and the equivalent mechanism between the nine-switch converter and the dual six-switch converter is first proposed. Furthermore, a mathematical model of the nine-switch converter based on the unipolar binary logic switching function is established. In order to simplify the mathematical model of the nine-switch-converter-based DFIG-WECS, the parameter mapping relationship between the nine-switch converter with loads and the nine-switch-converter-based DFIG-WECS under *dq* coordinate system is given. Meanwhile, the adaptive resonant proportional integral (PI) (AR-PI) current controller based on the resonant controller, the PI controller, and the adaptive genetic algorithm is applied for the DFIG wind generation system. As a result, harmonic current content, overshoot, and dynamic response speed of the nine-switch-converter-based DFIG-WECS have been significantly improved. Finally, the simulations and experimental results verify the validity and reliability of the proposed mathematical model and control algorithm.**

***Index Terms*—Current harmonics suppression, doubly-fed induction generator (DFIG), nine-switch converter, switching function, virtual leg.**

I. Introduction

AS A SOLUTION for supplying two sets of three-phase loads, nine-switch converter with nine switching devices and three-phase three-leg [1] has been proposed, as shown in Fig. 1. Generally, the nine-switch converter can realize the function of two-level rectifiers and inverters through the multiplexing of the switching tubes. However, compared with the conventional dual six-switch converters (SSC), the active switches are reduced by 25%, as well as the associated gating drivers, heatsinks, protection circuits, and snubbers can be reduced from 12 to 9. Thus, the volume of the converter is reduced, the power density of the converter is increased, and the structure of the system is simplified [1], [2]. Recently, nine-switch converter has been considered as a promising converter, which has been extensively studied and applied in many engineering applications, such as hybrid electric vehicles (EV) [2], [3], power conditioners [4], [5], torque control [6], [7], wind energy conversion systems (WECSs) [8], [9], uninterruptible power supply (UPS) [10], photovoltaic systems [11], and electrical machines [12], [13]. In the field of multiphase machine, it has been demonstrated that the nine-switch converter is an interesting option for a six-phase machine, especially the same frequency applied in the two three-phase output sets of the nine-switch converter [12].

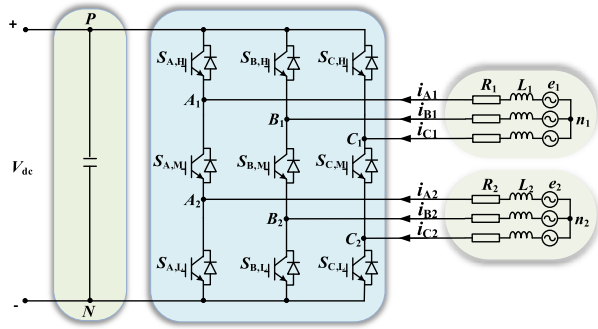

Fig. 1. Topology of the nine-switch converter.

According to the characteristics in different application fields of the nine-switch converter, various system mathematical models have been established [14]–[20]. For example, the system mathematical model of a nine-switch-converter-based fault ride-through topology for wind turbine applications is built by combining the output phase voltages of the nine-switch converter, the voltages and currents of the filter link, and the voltages of the grid side, which is used to enable shunt and series compensation in response to the system dynamics and grid faults [17]. Both sides' models are established with two side source voltages, capacitor voltages, and outputs currents of two ac terminals in the nine-switch converter to realize both sides' power flow regulation [18]. Nine-switch converter is equivalent to grid-side SSC and rotor-side SSC by time-shared strategy in a doubly fed induction generator (DFIG) wind power system,

Manuscript received August 3, 2019; revised October 17, 2019; accepted November 27, 2019. Date of publication December 5, 2019; date of current version March 13, 2020. This work was supported in part by Tianjin Science and Technology Support Project under Grant 15zczdsf00080, in part by Tianjin Key Scientific and Technological Support Projects under Grant 18YFZCSF00300, in part by Tianjin Education Commission Scientific Research Project under Grant 2017KJ059, in part by Tianjin Education Commission Scientific Research Project under Grant 2018KJ179, and in part by Tianjin Education Commission Scientific Research Project under Grant 2019KJ104. Recommended for publication by Associate Editor D. O. Neacsu. *(Corresponding author: Lei Pan.)*

The authors are with the School of Control and Mechanical Engineering, Tianjin Chengjian University, Tianjin 300384, China (e-mail: 1457101045@qq.com; meizijingjing@163.com; primepang@163.com; 295952769@qq.com; panlei4089@163.com).

Color versions of one or more of the figures in this article are available online at http://ieeexplore.ieee.org.

Digital Object Identifier 10.1109/TPEL.2019.2958425

and two independent output voltages are used to establish the system model with the parameters of the grid side and rotor side together [19].

From above discussion, the mathematical model of the nine-switch converter is not delved into the details, but the system model is established by using the output voltage/current of the nine-switch converter and other system parameters. In [20], the switching function model and the equivalent circuit model of the nine-switch converter have been built in $\alpha\beta$ coordinate system. But the model does not reflect the relationship between the phase voltages of the nine-switch converter and the binary logic states of the three legs. From the input side, the nine-switch converter is not equivalent to two constrained SSCs, and the equivalent relationship between the nine-switch converter and the SSC is not clarified. In addition, the model in the $\alpha\beta$ coordinate system is too complex. If the model is converted into the *dq* coordinate system, it will be more complex, and the coupling between the two output terminals is more serious. That is not conducive to the decoupling adjustment of active and reactive powers and control system design.

In view of the abovementioned problems, the concept of virtual leg is proposed, and the model of the nine-switch converter based on the unipolar binary logic switching function of virtual leg is established. In this model, the nine-switch converter is equivalent to dual constrained SSCs, and the decoupling of the upper and lower output terminals is realized. To verify the validity of the model, this model is applied in the DFIG-WECS.

Generally, in the DFIG wind system, the proportional integral (PI) controller based on grid voltage vector orientation is adopted to achieve dc bus voltage stability and adjust the power factor in the grid-side converter, and stator flux (or voltage)-oriented vector PI controller is used to realize active and reactive power regulation in the rotor-side converter [21]–[25]. In order to obtain good dynamic performance, cross-coupling terms and feedforward compensation terms related to temperature and circuit parameters are often introduced into the control system [21]–[23], which will affect the robustness of the control system. In addition, in order to compensate for the low-order harmonics, the PI control system needs complex high-low-pass filtering and coordinate transformation [24], [25], which will increase the amount of calculation and make the realization of the system control algorithm more difficult [26]. Therefore, an adaptive resonant PI (AR-PI) current controller is designed for the grid-side converter and rotor-side converter, respectively. The proposed controller has good harmonic suppression characteristics, excellent suppression interference performance, and fast dynamic response performance. Simultaneously, it can effectively reduce the filtering part and coordinate transformation of the system.

II. Modeling Analysis of Nine-Switch-Converter-Based DFIG-WECS

A. Mathematical Model of the Nine-Switch Converter

The nine-switch converter has three phases and three-legs, as shown in Fig. 1. Generally, this topology is treated as two independent converters, namely Con-U and Con-L, by sharing three middle devices.

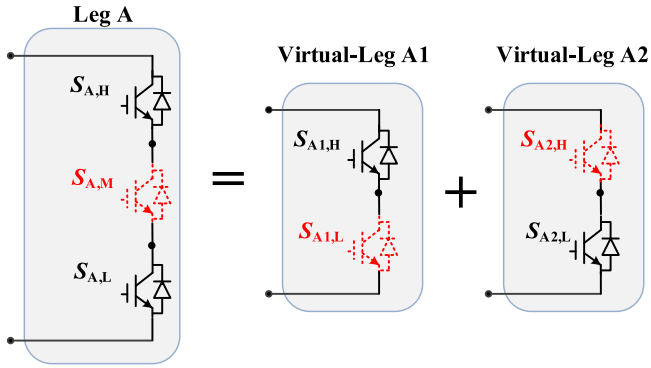

Fig. 2. Equivalent relationship between leg A and virtual-leg A.

In order to analyze and control the nine-switch-converter-based DFIG-WECS effectively, the nine-switch converter needs to be accurately modeled, and the established model will be based on the following assumptions.

1) The transistor and its body diode form an ideal switch, and switching times are zero.
2) The voltage of three-phase grid is balanced and stable, and the three-phase load in the system is symmetric completely.

First, the general mathematical model of the nine-switch converter is established by using the switching function. Each leg of the converter has three switches, and the gate signal of the midswitch is generated by the logical XOR of the upper and lower switches. Each switch has two different switching states that can be represented by a binary logic switching signal.

Normally, there are eight (2^3) kinds of switching states for each leg of the nine-switch converter. Since the output port cannot be floating, the dc bus cannot be short circuited. There are only three effective switching states for each leg. In consideration of the combination of the feasible state of three legs, there are total 27 (3^3) feasible switching states for the nine-switch converter. Then, the switching state of each leg was structured

$$\begin{cases} s_{ak} = (s_{\mathrm{A,M}} - s_{\mathrm{A,L}})_k \\ s_{bk} = (s_{\mathrm{B,M}} - s_{\mathrm{B,L}})_k \\ s_{ck} = (s_{\mathrm{C,M}} - s_{\mathrm{C,L}})_k \end{cases} \tag{1}$$

where, A, B, and C refer to legs A, B, and C, respectively; M and L refers to the mid and lower semiconductors, respectively; and s_{ik} (i = a, b, c; k = 0,1,2 …26) refers to the switching state of each leg.

Essentially, the middevice of the nine-switch converter is virtualized into two switches by multiplexing structure, and the nine-switch converter is equivalent to dual constrained SSCs. The relationship between leg A of the nine-switch converter and leg A of the two SSCs is shown in Fig. 2. The equivalent mechanism can be explained as

$$\begin{cases} s_{\mathrm{A,H}} = s_{\mathrm{A1,H}} = \overline{s_{\mathrm{A1,L}}} \\ s_{\mathrm{A,L}} = s_{\mathrm{A2,L}} = \overline{s_{\mathrm{A2,H}}} \\ s_{\mathrm{A,M}} = s_{\mathrm{A,H}} \oplus s_{\mathrm{A,L}} = s_{\mathrm{A1,H}} \oplus s_{\mathrm{A2,L}} = \overline{s_{\mathrm{A1,L}}} \oplus \overline{s_{\mathrm{A2,H}}} \end{cases} \tag{2}$$

TABLE I
THREE SWITCHING STATES PER PHASE (FOR LEG A)

State	Switching			Pole Voltages	
	$S_{\mathrm{A,H}}$	$S_{\mathrm{A,M}}$	$S_{\mathrm{A,L}}$	u_{A1}	u_{A2}
1	1	1	0	V_{dc}	V_{dc}
0	0	1	1	0	0
-1	1	0	1	V_{dc}	0

where, $s_{\mathrm{A}X,\mathrm{Y}}$ ($X = 1, 2$; $Y = \mathrm{H}, \mathrm{L}$) refers to the switches in virtual leg; $\oplus$ means the operation logic XOR; and $\overline{s_*}$ means the operation logic NOT.

Then, a concept of virtual leg, which is equivalent to the leg of a conventional SSC, is introduced for more effectively expound the equivalent mechanism between the nine-switch converter and the traditional dual SSCs. Hence, the operation mechanism of the nine-switch converter could be explained clearly

$$\begin{cases} S_{\mathrm{A}1} = |s_{\mathrm{a}k}| \\ S_{\mathrm{B}1} = |s_{\mathrm{b}k}| \\ S_{\mathrm{C}1} = |s_{\mathrm{c}k}| \\ S_{\mathrm{A}2} = (s_{\mathrm{a}k} + |s_{\mathrm{a}k}|)/2 \\ S_{\mathrm{B}2} = (s_{\mathrm{b}k} + |s_{\mathrm{b}k}|)/2 \\ S_{\mathrm{C}2} = (s_{\mathrm{c}k} + |s_{\mathrm{c}k}|)/2. \end{cases} \tag{3}$$

Considering the nine-switch converter topological constraint and switching states of per leg, as shown in Table I, the relationship between the pole voltage and virtual leg can be obtained

$$\begin{cases} u_{\mathrm{A}i} = V_{\mathrm{dc}} S_{\mathrm{A}i} \\ u_{\mathrm{B}i} = V_{\mathrm{dc}} S_{\mathrm{B}i} \\ u_{\mathrm{C}i} = V_{\mathrm{dc}} S_{\mathrm{C}i} \end{cases} \quad (i = 1 \text{ or } 2) \tag{4}$$

where V_{dc} and $u_{\mathrm{A}i}$ are dc-link voltages and phases Ai ($i = 1, 2$) to negative dc bus (n) voltages, respectively.

From Fig. 1, the converter voltages can be expressed in terms of load-neutral voltages and pole voltage as follows:

$$\begin{cases} u_{\mathrm{A}i} = u_{\mathrm{A}i,\mathrm{n}i} + u_{\mathrm{n}i} \\ u_{\mathrm{B}i} = u_{\mathrm{B}i,\mathrm{n}i} + u_{\mathrm{n}i} \\ u_{\mathrm{C}i} = u_{\mathrm{C}i,\mathrm{n}i} + u_{\mathrm{n}i} \end{cases} \tag{5}$$

where $u_{\mathrm{n}i}$ ($i = 1, 2$) and $u_{\mathrm{j}i,\mathrm{n}i}$ (j = A, B, C; $i = 1, 2$) are load-neutral voltages and phases voltages, respectively.

Supposing a balanced three-phase voltage for two ac terminals, then

$$u_{\mathrm{A}i,\mathrm{n}i} + u_{\mathrm{B}i,\mathrm{n}i} + u_{\mathrm{C}i,\mathrm{n}i} = 0. \tag{6}$$

From (4)–(6), it can be concluded that

$$u_{\mathrm{n}i} = (u_{\mathrm{A}i} + u_{\mathrm{B}i} + u_{\mathrm{C}i})/3 = V_{\mathrm{dc}}(S_{\mathrm{A}i} + S_{\mathrm{B}i} + S_{\mathrm{C}i})/3. \tag{7}$$

According to (4)–(7), the output voltage of this converter can be written in terms of the virtual leg

$$\begin{cases} u_{\mathrm{A}i,\mathrm{n}i} = V_{\mathrm{dc}}(2S_{\mathrm{A}i} - S_{\mathrm{B}i} - S_{\mathrm{C}i})/3 \\ u_{\mathrm{B}i,\mathrm{n}i} = V_{\mathrm{dc}}(-S_{\mathrm{A}i} + 2S_{\mathrm{B}i} - S_{\mathrm{C}i})/3 \\ u_{\mathrm{C}i,\mathrm{n}i} = V_{\mathrm{dc}}(-S_{\mathrm{A}i} - S_{\mathrm{B}i} + 2S_{\mathrm{C}i})/3. \end{cases} \tag{8}$$

By applying Kirchhoff's voltage law to Fig. 1, the differential equation of the nine-switch converter can be obtained as follows:

$$\begin{cases} L_i \frac{di_{\mathrm{A}i}}{dt} = -R_i i_{\mathrm{A}i} - e_{\mathrm{A}i} + u_{\mathrm{A}i,\mathrm{n}i} \\ L_i \frac{di_{\mathrm{B}i}}{dt} = -R_i i_{\mathrm{B}i} - e_{\mathrm{B}i} + u_{\mathrm{B}i,\mathrm{n}i} \\ L_i \frac{di_{\mathrm{C}i}}{dt} = -R_i i_{\mathrm{C}i} - e_{\mathrm{C}i} + u_{\mathrm{C}i,\mathrm{n}i} \end{cases} \tag{9}$$

where $e_{\mathrm{A}i}$ and $i_{\mathrm{A}i}$ are the back electromotive force (EMF) voltages and phase currents of the three-phase loads in the upper and lower terminals, respectively; and L_i and R_i are the inductances and resistances of the three-phase loads in the upper and lower terminals, respectively.

Substituting (8) into (9), it is also possible to obtain a switching function model based on virtual leg for a nine-switch converter

$$\begin{cases} L_i \frac{di_{\mathrm{A}i}}{dt} = -R_i i_{\mathrm{A}i} - e_{\mathrm{A}i} + \frac{1}{3} V_{\mathrm{dc}}(2S_{\mathrm{A}i} - S_{\mathrm{B}i} - S_{\mathrm{C}i}) \\ L_i \frac{di_{\mathrm{B}i}}{dt} = -R_i i_{\mathrm{B}i} - e_{\mathrm{B}i} + \frac{1}{3} V_{\mathrm{dc}}(-S_{\mathrm{A}i} + 2S_{\mathrm{B}i} - S_{\mathrm{C}i}) \\ L_i \frac{di_{\mathrm{C}i}}{dt} = -R_i i_{\mathrm{C}i} - e_{\mathrm{C}i} + \frac{1}{3} V_{\mathrm{dc}}(-S_{\mathrm{A}i} - S_{\mathrm{B}i} + 2S_{\mathrm{C}i}). \end{cases} \tag{10}$$

Typically, an alternative way to improve the performance of the control system is to use the *dq* transformation. The *dq* components are directly associated with the active (*d*) and reactive (*q*) powers; the decoupling regulation of active and reactive powers can be achieved by directly regulating the *dq* module. Hence, the nine-switch converter mathematical model based on the *dq* synchronous reference frame (SRF) are as follows:

$$\begin{cases} L_i \frac{di_{di}}{dt} = -R_i i_{di} + \omega_i L_i i_{qi} + u_{di} - e_{di} \\ L_i \frac{di_{qi}}{dt} = -\omega_i L_i i_{di} - R_i i_{qi} + u_{qi} - e_{qi} \end{cases} \tag{11}$$

where S_{di} and S_{qi} denote the duty cycles, $u_{di} = V_{\mathrm{dc}} S_{di}$ and $u_{qi} = V_{\mathrm{dc}} S_{qi}$ are two output terminal voltage of the nine-switch converter; $\omega_{1,2}$ denotes the angular frequency of the synchronous frame and can be different for each feeder; and $[e_{di}, e_{qi}]^T$ and $[i_{di}, i_{qi}]^T$ are the vectors of back-EMF voltages and phase currents, respectively.

From (11), it can be found that the mathematical model of the nine-switch converter based on virtual leg is consistent with the back-to-back pulsewidth modulation (PWM) converter [27]. It can be concluded from the mathematical model that the nine-switch converter can be equivalent to dual constrained SSCs essentially. With this model, the nine-switch converter can achieve better modulation and control.

B. Mathematical Model of the Nine-Switch-Converter-Based DFIG-WECS

The DFIG wind system based on the nine-switch converter is shown in Fig. 3. The stator of the DFIG is connected to the grid, and the rotor is connected to the grid through the nine-switch converter. In the following section, the rotor side and the grid side of the nine-switch-converter-based DFIG-WECS are analyzed and simplified, respectively.

1) Mathematical Model of Equivalent Rotor-Side Converter: In order to get an accurate DFIG system mathematical model, it is necessary to build the circuit equivalent of DFIG. Under the *dq* SRF, rotor variables are referred to the stator side. With the stator

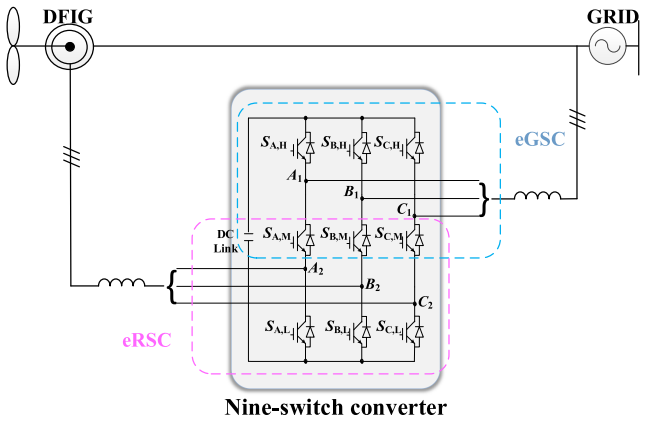

Fig. 3. Block diagram of the circuit diagram of the DFIG system based on the nine-switch converter.

voltage aligned to the *d*-axis of the *dq* SRF, the voltage equations of the stator windings and rotor windings are expressed as [21]

$$\begin{cases} u_{ds} = R_s i_{ds} + \frac{d\psi_{ds}}{\mathrm{d}t} - \omega_s \psi_{qs} \\ u_{qs} = R_s i_{qs} + \frac{d\psi_{qs}}{dt} + \omega_s \psi_{ds} \end{cases} \tag{12}$$

$$\begin{cases} u'_{dr} = R_r i'_{dr} + \frac{d\psi_{dr}}{\mathrm{d}t} - \omega_{sr} \psi_{qr} \\ u'_{qr} = R_r i'_{qr} + \frac{d\psi_{qr}}{dt} + \omega_{sr} \psi_{dr}. \end{cases} \tag{13}$$

Generally, the superscript $'$ means rotor variables referred to the stator side; u_s and u_r denote the stator and rotor voltages, respectively; i_s and i_r denote the stator and rotor currents, respectively; ψ_s and ψ_r denote the stator and rotor flux, respectively; R_s and R_r are the stator and rotor resistances of DFIG, respectively; ω_s represents synchronous electrical angular frequency; and ω_{sr} represents the slip angular frequency.

The flux linkages of stator and rotor windings under *dq* SRF are expressed as [25]

$$\begin{cases} \psi_{ds} = (L_{\mathrm{ls}} + L_m) i_{ds} + L_m i'_{dr} \\ \psi_{qs} = (L_{\mathrm{ls}} + L_m) i_{qs} + L_m i'_{qr} \end{cases} \tag{14}$$

$$\begin{cases} \psi_{dr} = (L_{lr} + L_m) i'_{dr} + L_m i_{ds} \\ \psi_{qr} = (L_{lr} + L_m) i'_{qr} + L_m i_{qs} \end{cases} \tag{15}$$

where L_{ls} and L_{lr} are the leakage inductances; and L_m is the mutual inductance between the stator and rotor.

By substituting (12), (14), and (15) into (13) and simplifying, the relationship between the rotor voltage and the rotor current can be obtained

$$\begin{cases} \sigma L_r \frac{di'_{dr}}{dt} = -R_r i'_{dr} + \omega_{sr} \sigma L_r i'_{qr} + u'_{dr} - e_{dr} \\ \sigma L_r \frac{di'_{qr}}{dt} = -\omega_{sr} \sigma L_r i'_{dr} - R_r i'_{qr} + u'_{qr} - e_{qr} \end{cases} \tag{16}$$

where $\begin{cases} L_s = L_{ls} + L_m \\ L_r = L_{lr} + L_m \end{cases}$, $\begin{cases} e_{dr} = L_m(u_{ds} - R_s i_{ds} + \omega_r \psi_{qs})/L_s \\ e_{qr} = L_m(u_{qs} - R_s i_{qs} - \omega_r \psi_{ds})/L_s \end{cases}$, and $\sigma = 1 - L_m^2/L_s L_r$ represents the total magnetic leakage coefficient; and ω_r represents the rotor electrical angular frequency and equals to $\omega_s - \omega_{sr}$.

By observing (16), it can be obtained that from the rotor winding perspective and taking the DFIG rotor-side as the virtual grid, e_r is considered as the virtual grid voltage, and $R_r + j\sigma\omega_{sr}L_r$ is regarded as the reactor parameters. Its equivalent circuit is shown in Fig. 4. Hence, the system can be considered as a standard three-phase PWM rectifier. The equivalent rotor-side converter (eRSC) emits a controllable voltage u_r. Moreover, by adjusting the amplitude and phase of u_r, the current i_r can be controlled. Simultaneously, the eRSC adjusts the active and reactive powers of the DFIG by controlling the active and reactive power components of the rotor current.

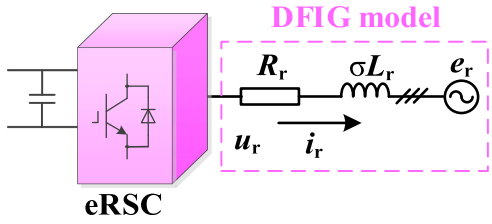

Fig. 4. Equivalent circuit diagram of the DFIG as the virtual grid.

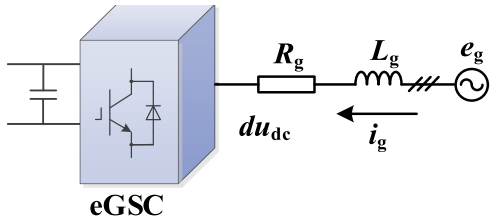

Fig. 5. Equivalent circuit diagram of the eGSC.

By comparing the DFIG mathematical model (16) with the nine-switch converter mathematical model (11), the following mapping relationship is obtained:

$$\begin{cases} L_1 = \sigma L_r \\ R_1 = R_r \\ \omega_1 = \omega_{sr} \\ i_{d1} = i'_{dr}, i_{q1} = i'_{qr} \\ u_{d1} = u'_{dr}, u_{q1} = u'_{qr} \\ e_{d1} = e_{dr}, e_{q1} = e_{qr}. \end{cases} \tag{17}$$

2) Mathematical Model of Equivalent Grid-Side Converter: As shown in Fig. 3, the grid-side branch Con-L of the nine-switch converter is connected to the grid e_g via the grid-connected inductor L_g and the equivalent resistor R_g, and its equivalent circuit is shown in Fig. 5. In the case when grid voltage direction is determined, the grid side can be described by the following circuit equation:

$$\begin{cases} L_g \frac{di_{dg}}{dt} = -R_g i_{dg} + \omega_g L_g i_{qg} - e_{dg} + d_d u_{\mathrm{dc}} \\ L_g \frac{di_{qg}}{dt} = -\omega_g L_g i_{dg} - R_g i_{qg} - e_{qg} + d_q u_{\mathrm{dc}} \end{cases} \tag{18}$$

where i_g is the output currents of ac side; and e_g denotes the grid voltage.

By comparing the mathematical model of this branch (18) with the nine-switch converter mathematical model (11), the

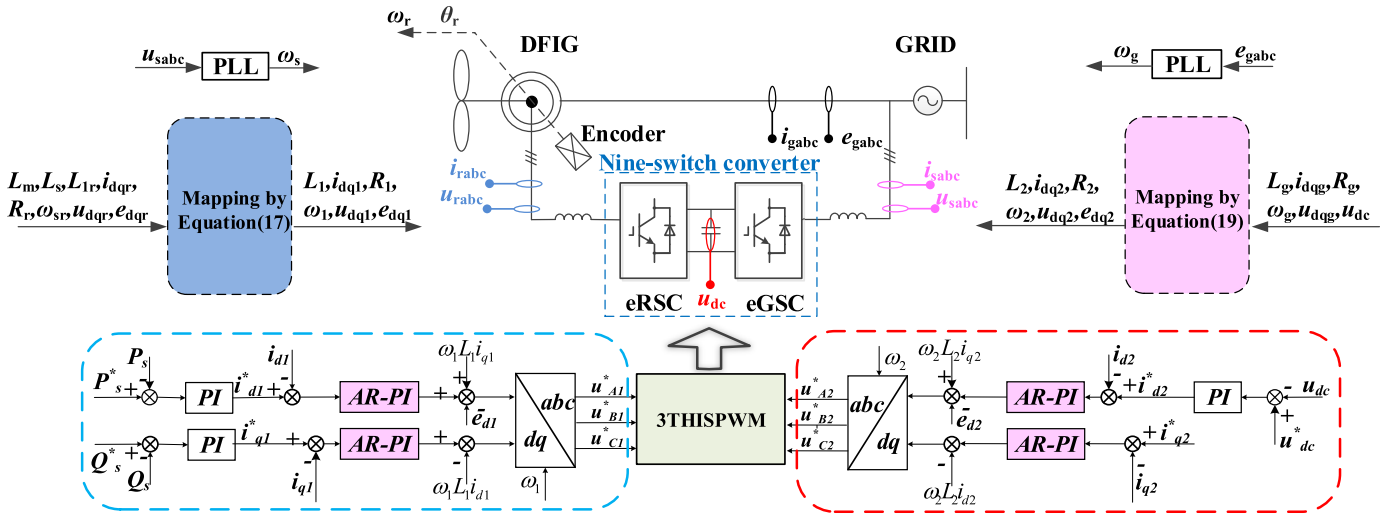

Fig. 6. Equivalent converter control block diagram.

mapping relationship is obtained as follows:

$$\begin{cases} L_2 = L_g \\ R_2 = R_g \\ \omega_2 = \omega_g \\ i_{d2} = i_{dg}, i_{q2} = i_{qg} \\ u_{d2} = d_d u_{\rm dc}, u_{q2} = d_q u_{\rm dc} \\ e_{d2} = e_{dg}, e_{q2} = e_{qg}. \end{cases} \tag{19}$$

Through the analysis and simplification presented in the previous section, the mathematical model of the nine-switch-converter-based DFIG-WECS can be unified into the mathematical model of (11). Meanwhile, the parameter mapping relationship between the two systems is given in detail. The aforementioned parameter mapping is the basis for the design of the nine-switch-converter-based DFIG-WECS. Through this model, the design of the system can be simplified effectively.

III. Control and Modulation of Nine-Switch-Converter-Based DFIG-WECS

In this section, the proposed control strategy is divided into two parts: 1) The regulation of active power and reactive power of DFIG is realized by the rotor-side rectifier (Con-U), whose purpose is to track the given active and reactive power instructions; at the same time, the current inner loop realizes the suppression of stator harmonic current. 2) The stability of the dc bus voltage and the output three-phase ac power quality are controlled by the grid-side inverter (Con-L).

The two cascaded control loops, as shown in the blue line block in Fig. 6, are designed to realize the stator harmonic current suppression and active and reactive power decoupling regulation. Similarly, the control structure in the red line block in Fig. 6 can implement the stability of the dc bus voltage and the power quality control of three-phase ac.

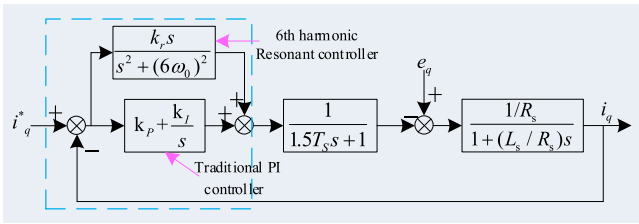

Fig. 7. Block diagram of current loop based on resonant-PI controllers.

A. Design and Implementation of Current Controller

In the nine-switch-converter-based DFIG-WECS, due to the dead-time effect of the converter and the effect of nonlinear loads on grid voltage, the three-phase current of the control system contains quite high harmonics components.

Among the total harmonic distortion (THD) of the system, the fifth and seventh harmonic components are the most prominent. After a Park transformation, these harmonics are equivalent to the sixth harmonic current [28]. In this article, a resonant controller with the six times of the working frequency ($\omega_6 = 6 * 2\pi f$) is used in parallel with a traditional PI controller to suppress the sixth harmonic components on the dq axis. The block diagram of the current loop based on resonant controllers with different resonant frequencies in the q frame is shown in Fig. 7.

In order to prove the correctness of the current loop based on the resonant controller, Fig. 8 shows the Bode diagram of the current loop in the simulation environment. From Fig. 8, it can be seen that when the frequency is 69 rad/s, the phase margin (PM) is 165° at point A, which is greater than 0°. It can also be seen that the PM at the resonant frequency is also greater than 0° at point B. In addition, the current loop based on the resonant-PI controller in Fig. 7 is a minimum-phase system. Therefore, the stability of the designed current loop based on the proposed controller is guaranteed.

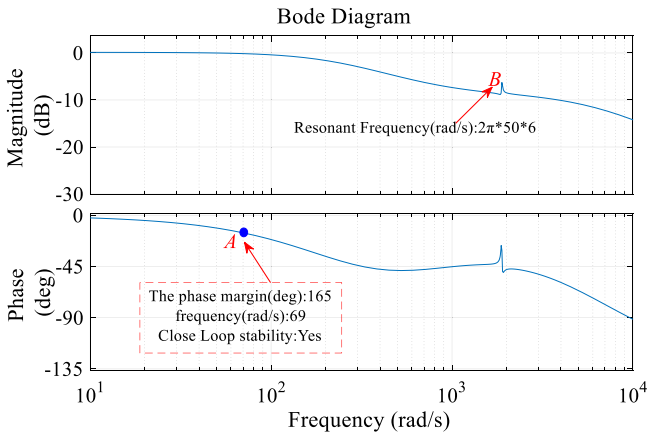

Fig. 8. Bode diagram of the current loop based on resonant-PI controllers.

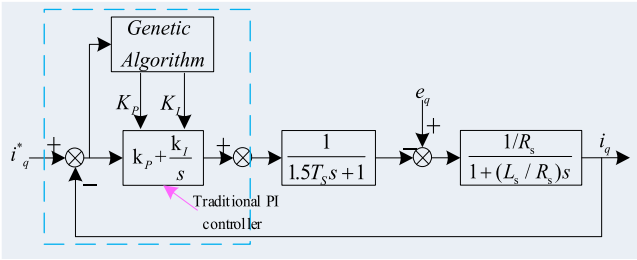

Fig. 9. Block diagram of current loop based on GA PI controllers.

Moreover, the conventional PI controller is quite difficult to achieve effective control for a complex nonlinear system and cannot simultaneously facilitate perfect tracking and disturbance rejection. Recently, the genetic algorithm (GA), which is a stochastic search method based on Darwinian survival-of-the-fittest theorem, has been applied to many engineering fields. By combining the GA and the PI control law, a GA–PI controller has been successfully developed, which is shown in Fig. 9.

GA is an artificial optimization algorithm that simulates natural evolution. It has been considered as function optimizers for solving complex nonlinear optimization problems [29]. The main procedures of GA are initial population, individual evaluation, selection and reproduction, crossover, and mutation, whereas the genetic operators, such as selection and crossover, are used to select the best individuals and update the population. The mutation operators are used for facilitating the exploration of the global search space to avoid premature convergence.

The flowchart of the parameter tuning process of resonant-PI controller based on a GA is shown in Fig. 10. The working principles of GA are described as follows.

Step 1: Create an initial population and encode in binary. The parameters K_P, K_I, and K_r of the resonant-PI controller are encoded as binary strings generally called chromosomes.

Step 2: Evaluate the fitness value of each chromosome. Simultaneously, select the fittest individuals of the population. The parent selection strategy is to use proportional roulette wheel selection.

Step 3: Using the dominants selected above, the crossover and mutation operators are applied to operate the population to produce the next generation population. In our case, a single point crossover is used, and the crossover probability is $P_c = 0.9$; the mutation probability uses the adaptive probability $P_m = 0.01 - [1:1:\text{size}] \times (0.01)/\text{size}$ to perform individual genetic variation. The parameters used to initialize the GA algorithm parameters are defined in Table II.

Step 4: Go to step 2 until the parameters converge or reach a predetermined target.

In the normal way, the fitness value is a number that indicates the goodness of each chromosome and is evaluated by an objective function. Various objective functions have been used in [29], and in this study, the objective function is defined as follows:

$$J = \alpha * \text{overshoot} + \beta * \text{ISE} \tag{20}$$

where $\text{ISE} = \int_0^\infty e^2(t)dt$ means integral of squared error, and overshoot $= \max(i_q) - i_q^*$, we choose $\alpha = \beta = 0.5$ for no preference between the two objectives.

In order to obtain the optimal parameter combination of the resonant-PI controller, the controller parameters are repeatedly evaluated by the GA in the offline state. The obtained sets of optimal parameter combinations are shown in Table III. These parameters can be used when the system is running online.

On the basis of the analysis of above, combining the resonant controller, PI controller, and adaptive GA, an AR-PI current controller is proposed, and its overview diagram is depicted in Fig. 10. The proposed AR-PI current controller obtains the optimal parameters of the controller, which could reduce the harmonic content and the overshoot effectively.

In order to test the current dynamic performance and interference suppression capabilities of the proposed controller, the system runs in a current loop. The reference current i_q^* is set to a step change signal of 0 to 1 A, and noise interference with a range between -0.3 and 0.3 A is added at 2.5 s. Fig. 11 shows the comparison results between the PI controller, the resonant-PI controller, and the AR-PI controller. It can be seen that the settling time of the AR-PI controller is smaller than the others. When the system is disturbed, the current fluctuations of the AR-PI controller are obviously less than the resonant-PI controller and are far less than the PI controller.

B. eRSC Control Strategy

Rotor-side control consists of two cascaded control loops; the outer loop is used to adjust active and reactive powers, and the inner loop is used to regulate the rotor current with AR-PI.

In the case of the stator, voltage (also the grid voltage) is aligned with the *d*-axis of the *dq* SFR, and the active power and reactive power [21] outputs of the stator side are

$$\begin{cases} P_s = \frac{3}{2} u_{ds} i_{ds} = -\frac{3}{2} \frac{u_{ds} L_m}{L_s} i'_{\text{dr}} \\ Q_s = -\frac{3}{2} u_{ds} i_{qs} = \frac{3}{2} \left(\frac{u_{ds}^2}{\omega_1 L_s} + \frac{u_{ds} L_m}{L_s} i'_{qr} \right). \end{cases} \tag{21}$$

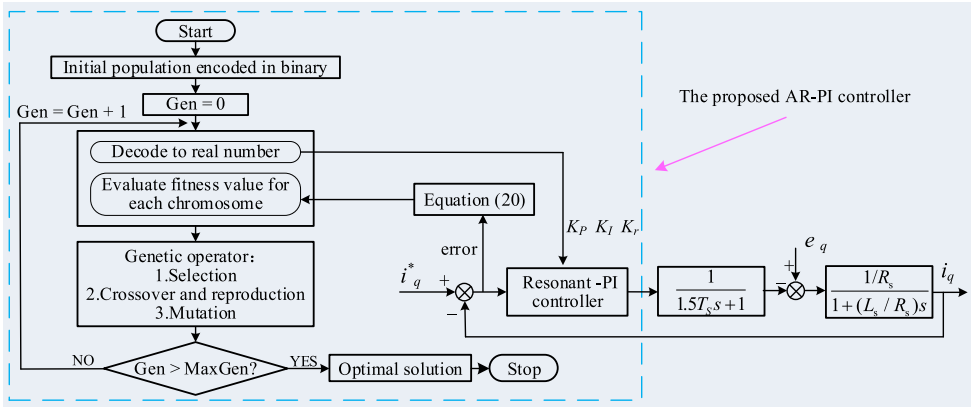

Fig. 10. Detailed block diagram of the current loop based on the AR-PI controller.

TABLE II
GA PARAMETERS

Description	parameters
Population size	20
Maximum iteration	50
Crossover probability	0.9
Mutation probability	P_m
Number of bits per chromosome	16

TABLE III
OPTIMUM SET OF RESONANT-PI CONTROLLER PARAMETERS

optimal set	K_P	K_I	K_r
Set1	14.77	0.84	200
Set2	6.72	0.37	160
Set3	5.45	0.15	125

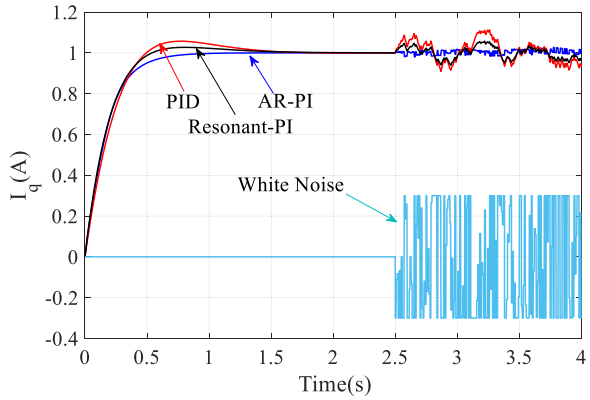

Fig. 11. Comparison results of current dynamic performances between different current controllers.

Moreover, rotor current i'_{dr}, i'_{qr} can be calculated from the active power and reactive power of stator side as [21]

$$\begin{cases} i'_{dr} = \frac{2P_s L_s}{3u_{ds}L_m} \\ i'_{qr} = -\frac{2Q_s L_s}{3u_{ds}L_m} - \frac{u_{ds}}{\omega_s L_m}. \end{cases} \tag{22}$$

According to (17), (21), and (22), the current inner loop and power outer loop control block diagram of the rotor-side equivalent converter is shown in Fig. 6.

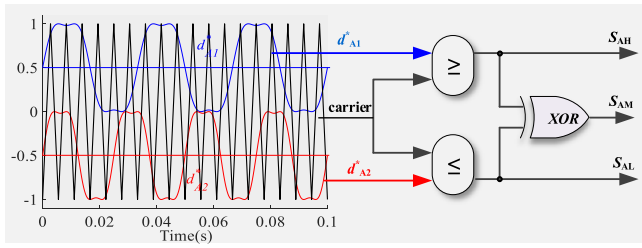

Fig. 12. PWM modulation strategy of the nine-switch converter (for leg A).

C. Equivalent Grid-Side Converter Control Strategy

The same as the rotor side, the grid side is also divided into two cascaded control loops, and they are the dc voltage control inner loop and grid current control outer loop in Fig. 6.

D. Modulation Algorithm Based on Third Harmonic Injection

In the linear modulation area of conventional sinusoidal pulsewidth modulation (SPWM), in order to enhance the utilization of the dc bus voltage, the principle of third-harmonic injection could be implemented. The typical SVPWM is a result of regular sampling after adding zero-sequence components to the phase-modulated wave of SPWM. Under the same circumstance, the SPWM modulation of the third harmonic injection has the same performance as the SVPWM, but it is easier to implement. Therefore, it is recognized as a technique that is more effortless than its counterparts. When the amplitude of the third harmonic injection is one-sixth of the reference fundamental, the voltage amplitude of the fundamental wave is increased by 15.48% compared with the conventional SPWM modulation algorithm [30]. Therefore, its third harmonic expression can be define as

$$u_{3h} = -\frac{u_{\mathrm{ref}}}{6}\sin 3\theta \tag{23}$$

where the expression $u_{\mathrm{ref}i} = \sqrt{u^{*2}_{di}+u^{*2}_{qi}}$ as the third harmonic amplitude.

In order to avoid the crossover between upper and lower reference signals per phase, as shown in Fig. 12, it is necessary to add a suitable dc offset value to meet the limitations imposed by its

TABLE IV
PARAMETERS OF THE 4-KW DFIG SYSTEM

PARAMETERS	Value	Per Unit
Number of pole-pairs p	3	
Grid-connected Transformer	150 V/311 V(△/Y)	
Grid voltage/Frequency	311 V/50 Hz	
Stator resistance R_s	1.2 Ω	0.057
Rotor resistance R_r	1.5 Ω	0.071
Stator inductance L_s	136 mH	2.078
Rotor inductance L_r	138 mH	2.103
Mutual inductance L_m	133 mH	2.027
Grid-side inductance L_g	2 mH	0.01
Grid-side resistance R_g	0.01 Ω	0.0002
Slip angular frequency s_w	-0.3~0.3	

own multiplexing structure, and the suitable dc components are $u_{\text{offset},H} = 1 - M_H \frac{\sqrt{3}}{2}$ and $u_{\text{offset},L} = 1 - M_L \frac{\sqrt{3}}{2}$ Therefore, its duty cycle expression of upper and lower can defined as

$$\begin{cases} d^*_{\text{A1}} = u^*_{\text{A1}} + \frac{u_{\text{ref},H}}{6}\sin 3\theta + u_{\text{offset},H} \\ d^*_{\text{B1}} = u^*_{\text{B1}} + \frac{u_{\text{ref},H}}{6}\sin 3\theta + u_{\text{offset},H} \\ d^*_{\text{C1}} = u^*_{\text{C1}} + \frac{u_{\text{ref},H}}{6}\sin 3\theta + u_{\text{offset},H} \end{cases} \tag{24}$$

$$\begin{cases} d^*_{\text{A2}} = u^*_{\text{A2}} + \frac{u_{\text{ref},L}}{6}\sin 3\theta - u_{\text{offset},L} \\ d^*_{\text{B2}} = u^*_{\text{B2}} + \frac{u_{\text{ref},L}}{6}\sin 3\theta - u_{\text{offset},L} \\ d^*_{\text{C2}} = u^*_{\text{C2}} + \frac{u_{\text{ref},L}}{6}\sin 3\theta - u_{\text{offset},L} \end{cases} \tag{25}$$

where u_1^* and u_2^* are fundamental sinusoidal modulation waves of upper and lower terminals, respectively; and M_H and M_L are modulation indices of upper and lower terminals, respectively.

Fig. 12 shows the modulation waveform of three switches in one leg of the nine-switch converter, and the modulating wave is compared with the triangular carrier wave. When the modulation wave at the upper terminal is greater than the carrier wave, the upper switch drive signal is "1"; otherwise it is "0." On the contrary, when the modulation wave at the lower terminal is greater than the carrier wave, the lower switch drive signal is "0"; otherwise, it is "1." Mid switch drive signal is generated by the logical XOR of the upper and lower switches. Subsequently, the right side of Fig. 12 shows the available gating signals for the leg A of the nine-switch converter.

IV. Simulation and Experimental Results

In order to verify the theoretical analysis mentioned above and the correctness of the proposed control strategy, a DFIG with a rated power of 4 kW is taken as an example for simulation and experiment. In this section, the simulation results and experimental results of the nine-switch-converter-based DFIG-WECS are given. The system parameters in simulations and experiments are given in Table IV.

A. Simulation Results

Under the third harmonic injection modulation scheme described in Section III-D, the simulations for the nine-switch-converter-based DFIG-WECS are operating by MATLAB/Simulink. The simulation waveforms of the nine-switch-converter-based DFIG-WECS by using the proposed AR-PI current controller are shown in Figs. 13–16. For comparison, the simulation of the nine-switch-converter-based DFIG-WECS based on the traditional PI current controller is also established under the same parameters.

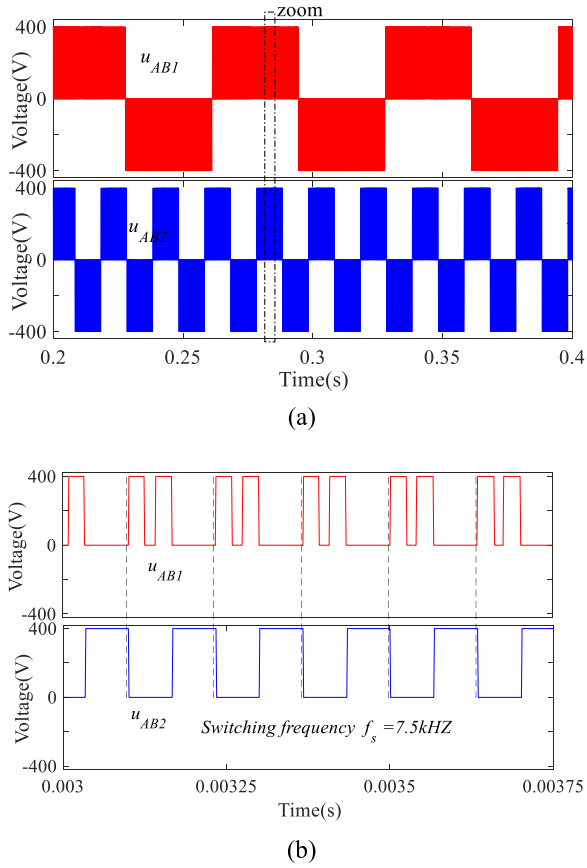

Fig. 13. Simulation waveforms of the PWM voltages in steady state. (a) Output PWM voltage of eRSC and eGSC. (b) Zoom-in view within a dotted line.

The voltage amplitude at the grid side was selected to be 311 V. Inner rotor current references can be calculated from (21), and they are 8.35 A and −7.089 A, respectively.

Fig. 13 shows the PWM voltage waveforms of the eRSC and equivalent grid-side converter (eGSC) outputs under the stability of the nine-switch-converter based DFIG-WECS. The PWM voltage in Fig. 13(a) shows that the eRSC and eGSC have been correctly modulated and the fundamental frequency of the PWM voltage is different. The local magnification in Fig. 13(b) indicates that the two sets of PWM voltages of the nine-switch converter do not overlap during one switching cycle under the unique modulation method of the nine-switch converter. Moreover, it is clearly shown that the switching period T_s of u_{AB1} and u_{AB2} remains constant, which is about 133.3 μs.

In the simulation, the DFIG works at supersynchronous speed, and the slip angular frequency s_ω is −0.3. The grid-connection mode of DFIG is no-load cutting-in. At the moment of 0.28 s, the active power instruction is suddenly reduced to 0.5 times of the original, and the reactive power remains unchanged.

Fig. 14 shows the waveforms of the stator and rotor currents, the active and reactive powers of the stator, and the dc bus voltage. By comparing Fig. 14(a) with 14(b), it can be obviously

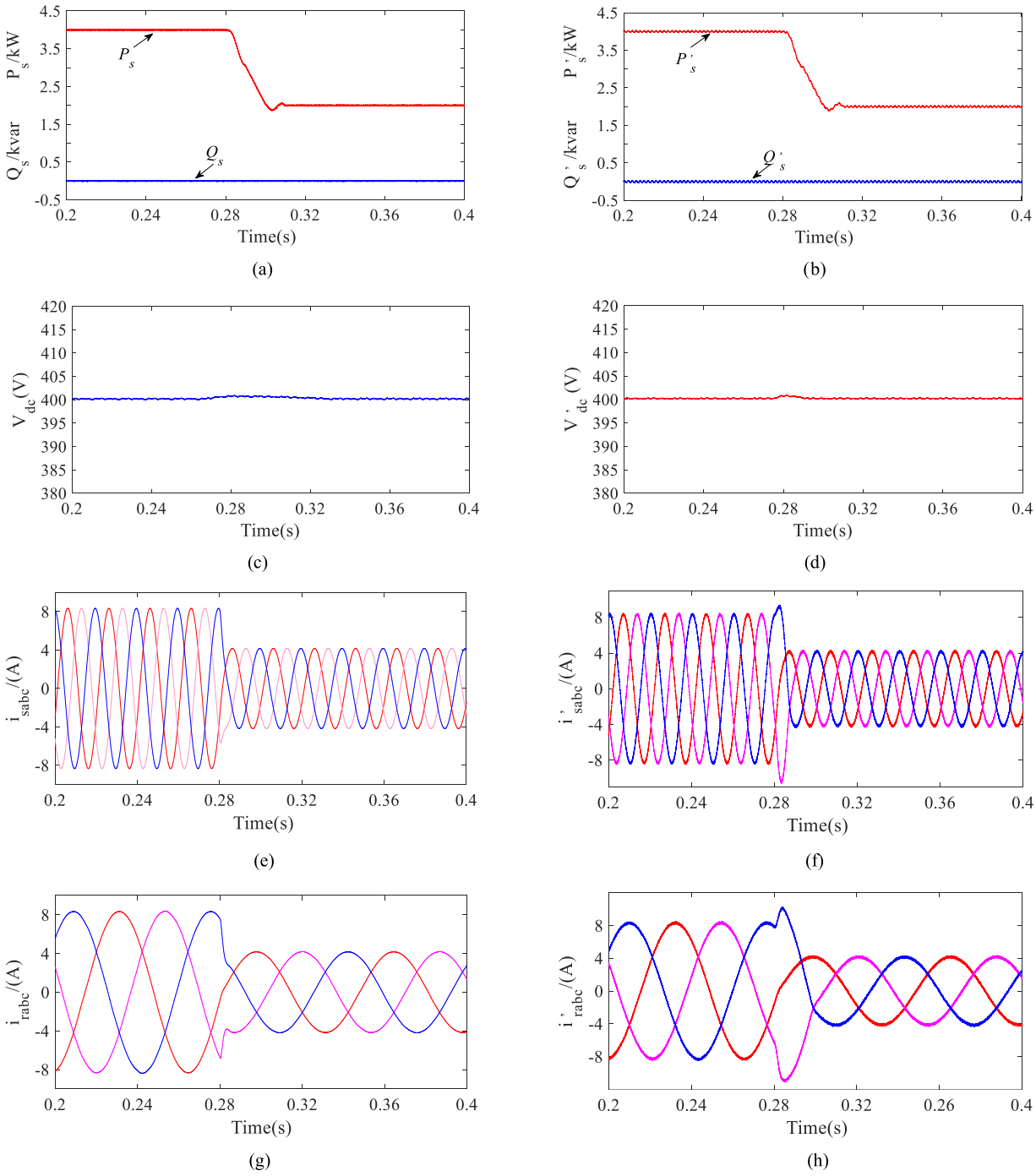

Fig. 14. Comparison results between different current controllers. (a) and (b) Active power and the reactive power. (c) and (d) DC bus voltage. (e) and (f) Stator three-phase current waveform. (g) and (h) Rotor three-phase current waveform.

seen that the proposed AR-PI controller can track active power quickly. By comparing Fig. 14(c) with 14(d), when the AR-PI controller is utilized, it can be seen that the dc bus voltage is controllable, and the dc bus voltage immediately recovers after the $V_{\rm dc}$ fluctuation occurs. Moreover, by comparing Fig. 14(e) and (g) with Fig. 14(f) and (h), respectively, it can be concluded that the proposed AR-PI controller can avoid the current overshoot and provide superior dynamic performance of current loop for the whole system. Thus, the effectiveness of the proposed AR-PI controller is confirmed.

Fig. 14(e) shows the stator currents i_{sa}, i_{sb}, and i_{sc} when a conventional PI controller is utilized, and as a comparison, Fig. 14(f) shows the stator currents when the proposed controller is utilized in the same simulation environment. Simultaneously, in order to verify the good harmonic suppression characteristics of the proposed controller, the fast Fourier transform (FFT)

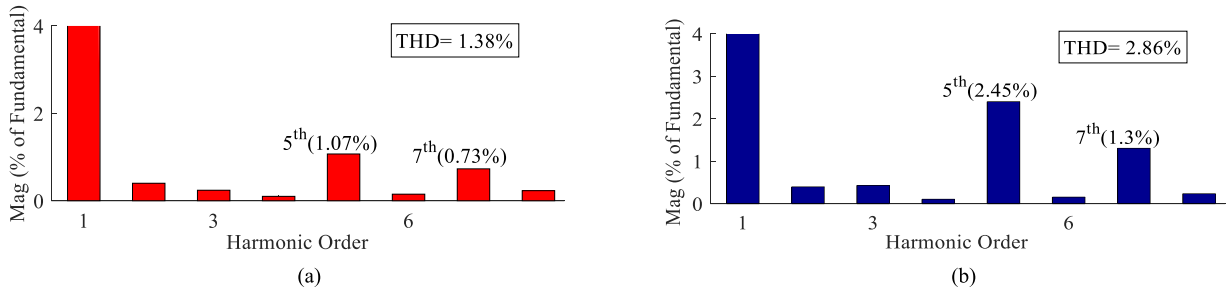

Fig. 15. Spectrum of stator current (a) with AR-PI controller and (b) with traditional PI controller.

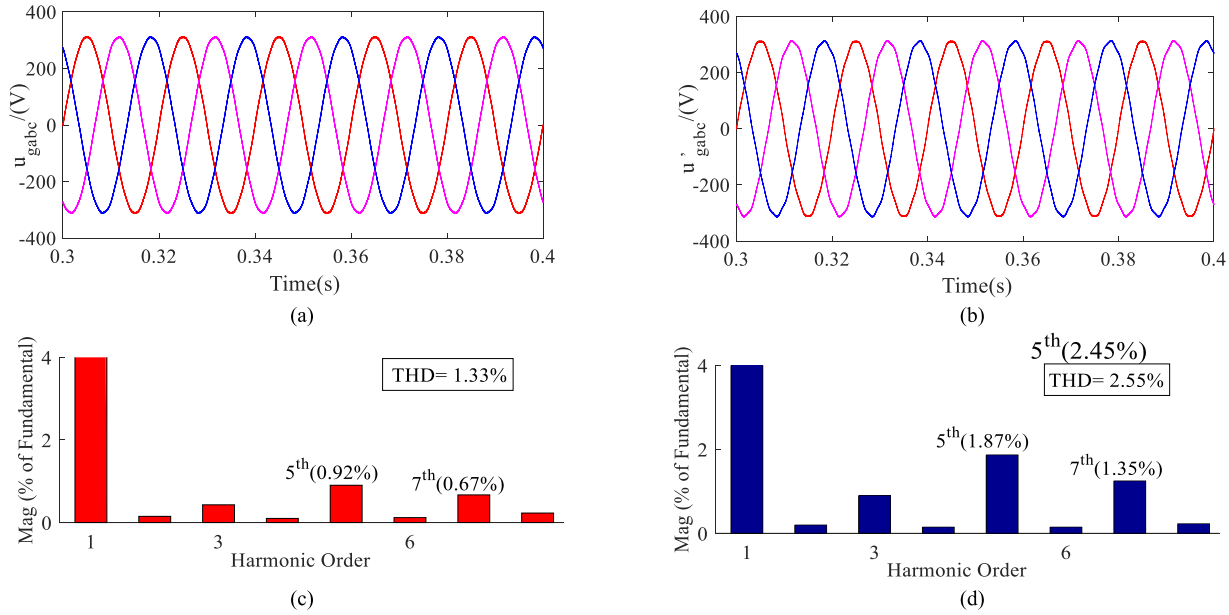

Fig. 16. Grid voltage and its spectrum analysis (a) and (c) with AR-PI controller, and (b) and (d) with traditional PI controller.

analysis module in SIMULINK is used to analyze the THD of the rotor current i_{sa}. The analysis results are shown in Fig. 15.

After the FFT spectrum analysis, the current spectrum diagram of stator current i_{sa} can be obtained and is shown in Fig. 15. By analyzing Fig. 15(a), it can be clearly seen that the harmonic amplitude of stator current i_{sa} is large at the fifth and seventh frequency orders. Comparing Fig. 15(b) with Fig. 15(a), it can be concluded that the current harmonic performance is effectively improved after using the AR-PI controller. And the THD is decreased from 2.86% to 1.38%, approximately 51.7%. In addition, the fifth and seventh harmonic components, which have a great influence on the harmonic content of stator current, are effectively suppressed. Among them, the fifth-order harmonic content is decreased by 56.3% from 2.45% to 1.07%, and the seventh-order harmonic content is decreased by 43.8% from 1.3% to 0.73%. Therefore, the harmonic suppression characteristic of the controller is verified effectively.

Fig. 16 shows the simulation results of the grid voltage, and its FFT spectrum is analyzed under different controllers, respectively. By comparing Fig. 16(a) and (c) with Fig. 16(b) and (d), respectively, it can be clearly seen that the proposed current controller has better performance of the grid voltage harmonic than that of traditional PI controller. At the same time, according to *IEEE 519* standard, the grid voltage harmonic performance meets the requirement that the THD injected by distributed generation units into a distribution network.

Simulation results have demonstrated the excellent performance of the proposed controller, such as an excellent current response, reduced the harmonic content of the DFIG, and low harmonic content of grid voltage.

B. Experimental Verification

To further demonstrate the theoretical analysis and the proposed control methods, a nine-switch-converter-based DFIG experimental system is developed. Experimental implementation of the proposed system has been achieved using a TMS320F2812 digital signal processor R&D board, a nine-switch converter, and a scaled DFIG with 4-kW rating power, as per the system parameters presented in Table IV. The schematic diagram of the experimental system is shown in Fig. 17. In the experimental system, the prime mover is an induction motor

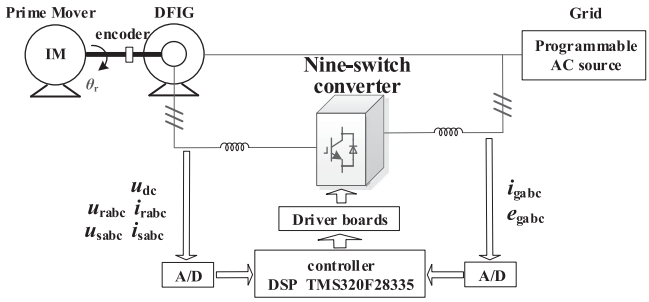

Fig. 17. Schematic diagram of the experiment system.

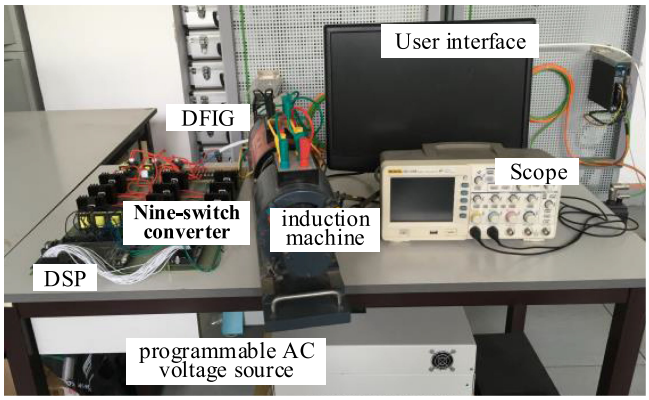

Fig. 18. Experimental platform.

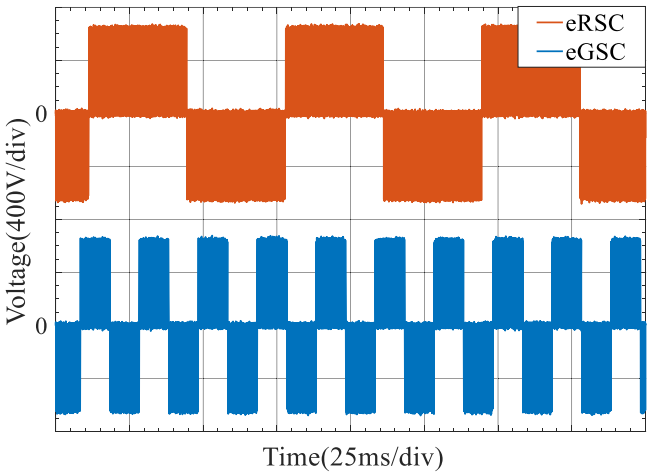

Fig. 19. Experimental PWM voltages in steady state.

that plays the role of a wind turbine emulator. A three-phase programmable ac voltage source was used to simulate the harmonic distorted power grid. It is worth noting that the sampling frequencies are chosen equal to 7.5 kHz, and the insulated gate bipolar translator (IGBT) switching frequencies are set at 7.5 kHz. The photograph of the experimental platform is shown in Fig. 18.

Fig. 19 shows the PWM voltage experimental waveforms of the eRSC and eGSC outputs under the stable state of the nine-switch-converter-based DFIG-WECS. The PWM voltage outputs in Fig. 19 show that the test prototype can operate correctly. To get a dynamic performance of the system, the active power of the system was changed from 4.0 to 2.0 kW. And the active power and reactive power of the system are shown in Fig. 20. It can be seen that the active/reactive power fluctuation of the DFIG stator is significantly suppressed. Tracking time of the proposed AR-PI controller is much shorter than that of the conventional PI controller. Moreover, the overshoot of the proposed AR-PI controller is much smaller than that of the conventional PI controller. It demonstrates that the proposed controller has better dynamic performance than that of the conventional PI controller.

Fig. 21(a) and (b) shows experimental waveforms of stator and rotor currents in two different experimental environments, respectively. It can be seen from Fig. 21(a) that when DFIG active power is changed, some irregularity and harmonic distortion of stator and rotor currents are reduced under the proposed control strategy. In addition, stator currents and rotor currents have better overshoot performance at the time of power mutation. Fig. 22(a) and (b) shows the harmonic characteristics of the stator current before the power changes. Correspondingly, Fig. 22(c) and (d) shows the harmonic characteristics of the stator current after the power changes. As can be seen, once the AR-PI controller is enabled, the fifth and seventh harmonic components of stator current can be effectively suppressed. Through the harmonic analysis by the power analyzer, the value changes of the fifth harmonics, fifth harmonics, and THD are shown in Table V. Therefore, it can be proved that the proposed AR-PI controller could work effectively under the grid voltage distortion. The sinusoidal DFIG stator current can be realized due to the excellent harmonic suppression capability of the controller.

Fig. 23(a) and (b) shows experimental waveforms of the grid voltage and dc bus voltage in two different experimental environments, respectively. With the AR-PI controller in Fig. 23(a), it can be seen clearly that the ripple of dc bus voltage is reduced relative to the scenario using the traditional PI controller. The harmonic content of grid voltage is also obviously reduced. As is shown in Fig. 24, through the harmonic analysis of the grid voltage by the power analyzer, it can be seen that once the AR-PI controller is enabled, the THD of the grid voltage can be effectively decreased from 4.04% to 2.93%, approximately 34.1%. Among them, the fifth-order harmonic content is decreased by 30.0% from 2.76% to 1.96%, and the seventh-order harmonic content is decreased by 46.83% from 2.52% to 1.34%.

All the experimental results can corroborate the feasibility of the proposed mathematical model of the nine-switch converter based on the virtual leg and the superiority of the system control strategy. Comparing to the systems in [2], [13], and [19], the performance evaluation is shown in Table VI.

However, there are other reasons for the increase in the THD in the three-phase current of the system. For example, due to the structure of the nine-switch converter itself, the eGSC and eRSC in Fig. 3 are interdependent. Therefore, the circulating current will flow in the system. The circulating current is also responsible for the increase in the THD of the three-phase current [31]. According to the state of the switch, the circulating current

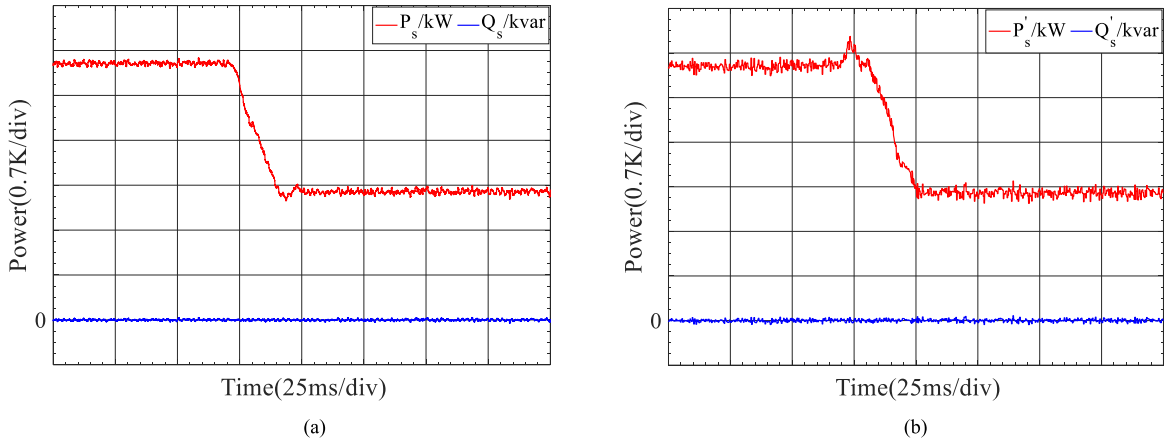

Fig. 20. Experimental waveform of active power and the reactive power (a) with AR-PI controller and (b) with traditional PI controller.

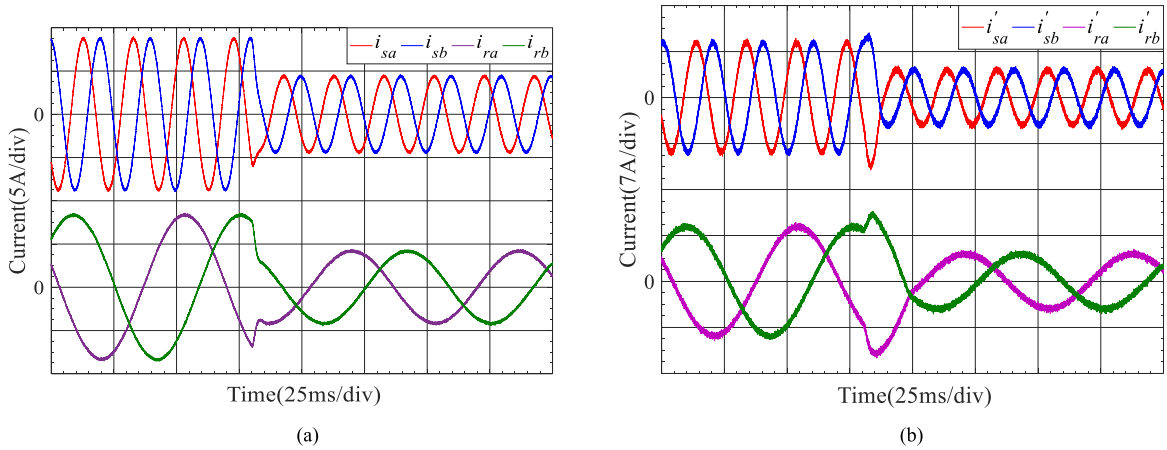

Fig. 21. Experimental two-phase current waveform of stator and rotor (a) with AR-PI controller and (b) with traditional PI controller.

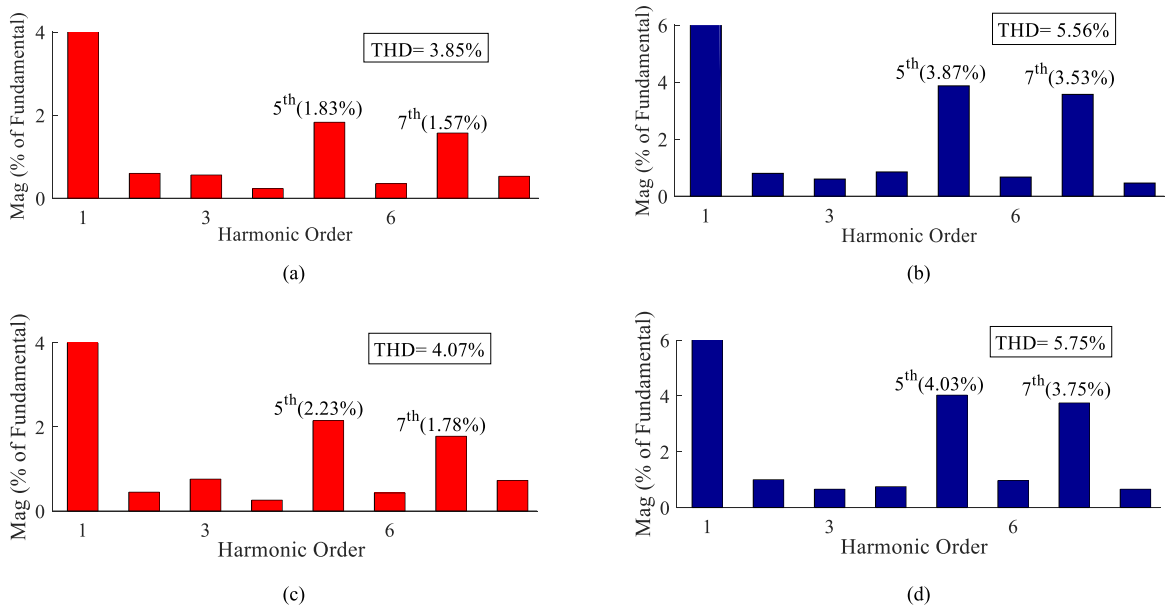

Fig. 22. Experimental stator current spectrum (a) and (c) with AR-PI controller, and (b) and (d) with traditional PI controller.

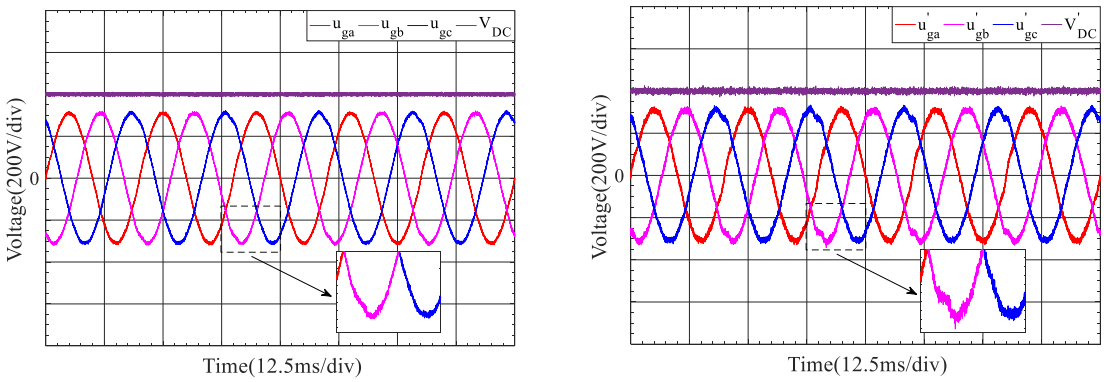

Fig. 23. Experimental results of dc bus voltage and grid voltage (a) with AR-PI controller and (b) with traditional PI controller.

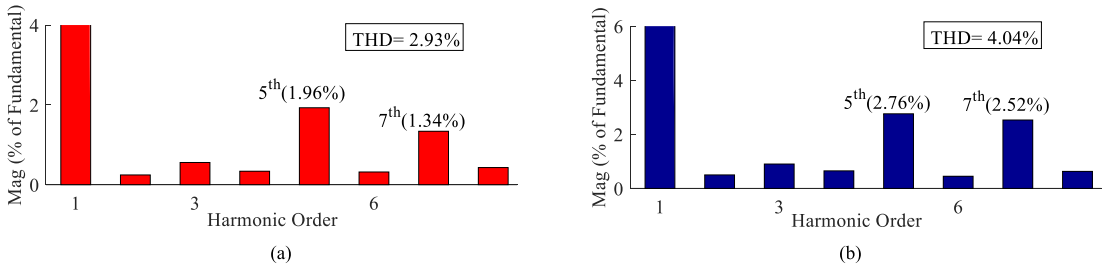

Fig. 24. Experimental grid voltage spectrum (a) with AR-PI controller and (b) with traditional PI controller.

TABLE V
COMPARISON OF STATOR CURRENT EXPERIMENTAL RESULTS

Operating points	Before power changes		After power changes	
Controller	AR-PI	PI	AR-PI	PI
THD	3.85%	5.56%	4.07%	5.75%
5th harmonic	1.83%	3.87%	2.23%	4.03%
7th harmonic	1.57%	3.53%	1.78%	3.75%

TABLE VI
COMPARISON OF PERFORMANCE EVALUATIONS

Comparison	Ref. [13]	Ref. [2]	Ref. [19]	Proposed
Application	Motor	Hybrid EV	WECS	WECS
Systems model	YES	YES	YES	YES
Nine-switch converter ontology model	NO	NO	NO	YES

EV: Electric Vehicle

can be divided into two types. One case is the zero-sequence circulating current shown in Fig. 25(a), and the other case is the cross current shown in Fig. 25(b). In addition, the circulating current may also cause switching losses of the nine-switch converter and large thermal and mechanical oscillations occur around the synchronous speed of the system [31].

In the following work, the influences of circulating current in the system and the strategies to suppress circulating current will be considered and become the focus of the next study.

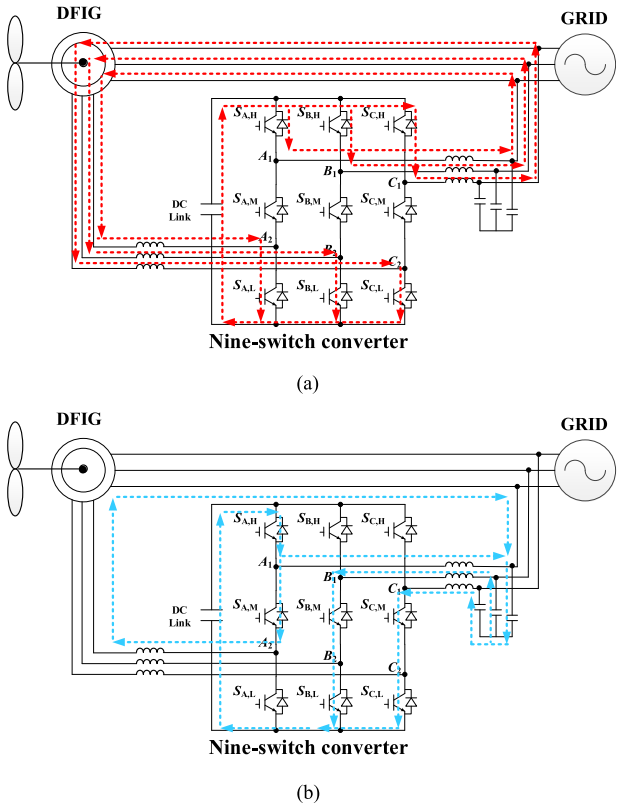

Fig. 25. Circulating current paths. (a) Zero-sequence circulating current path. (b) Cross current paths.

V. Conclusion

This article presents the architecture of a DFIG wind system based on a nine-switch converter. First, a switching function model of nine-switch converter based on the virtual leg is established; this model can realize independent decoupling control of the upper and lower terminals. Then, in order to suppress the harmonics of stator current and grid voltage, a new current controller named AR-PI current controller is proposed. Finally, simulation results show the superior control performance of the system, and the experimental results of the prototype also verify the abovementioned analysis results. There are three main contributions in this article.

1) The concept of virtual leg is proposed, and a mathematical model of a nine-switch converter based on unipolar binary logic switching function of virtual leg is established.
2) Through the analysis and simplification, the model of the nine-switch-converter-based DFIG-WECS was mapped into the mathematical model of the nine-switch converter to simplify the control process and improve control performance.
3) A control method based on the AR-PI controller is proposed to suppress the harmonic component of stator current and can improve the power quality of the grid. In addition, the controller has fast dynamic response performance.

References

[1] Z. Qin, P. C. Loh, and F. Blaabjerg, "Application criteria for nine-switch power conversion systems with improved thermal performance," *IEEE Trans. Power Electron.*, vol. 30, no. 8, pp. 4608–4620, Aug. 2015.

[2] H. Bizhani, G. Yao, S. M. Muyeen, S. M. Islam, and L. Ben-Brahim, "Dual mechanical port machine based hybrid electric vehicle using reduced switch converters," *IEEE Access*, vol. 7, pp. 33665–33676, Mar. 2019, doi: 10.1109/ACCESS.2019.2903765.

[3] S. M. Dehghan, M. Mohamadian, and A. Yazdian, "Hybrid electric vehicle based on bidirectional Z-source nine-switch inverter," *IEEE Trans. Veh. Technol.*, vol. 59, no. 6, pp. 2641–2653, Jul. 2010.

[4] L. Zhang, P. C. Loh, and F. Gao, "An integrated nine-switch power conditioner for power quality enhancement and voltage sag mitigation," *IEEE Trans. Power Electron.*, vol. 27, no. 3, pp. 1177–1190, Mar. 2012.

[5] S. Vinnakoti and V. R. Kota, "SRF and real power theory based control of a nine switch converter based UPQC," in *Proc. Int. Elect. Eng. Congr.*, 2017, pp. 1–4.

[6] M. S. Diab, A. A. Elserougi, A. S. Abdel-Khalik, A. M. Massoud, and S. Ahmed, "A nine-switch-converter-based integrated motor drive and battery charger system for EVs using symmetrical six-phase machines," *IEEE Trans. Ind. Electron.*, vol. 63, no. 9, pp. 5326–5335, Sep. 2016.

[7] C. N. Jibhakate, M. A. Chaudhari, and M. M. Renge, "Reactive power compensation using induction motor driven by nine switch AC–DC–AC converter," *IEEE Access*, vol. 6, pp. 1312–1320, Dec. 2018, doi: 10.1109/ACCESS.2017.2778291.

[8] M. R. Banaei and A. R. Dehghanzadeh, "Wind farm based doubly fed induction generator using a novel AC/AC converter," in *Proc. Power Electron., Drive Syst. Technol. Conf.*, 2011, pp. 398–402.

[9] M. Heydari, A. Yazdian Varjani, M. Mohamadian, and H. Zahedi, "A novel variable-speed wind energy system using permanent-magnet synchronous generator and nine-switch AC/AC converter," in *Proc. Power Electron., Drive Syst. Technol. Conf.*, 2011, pp. 5–9.

[10] C. Liu, B. Wu, N. Zargari, and D. Xu, "A novel nine-switch PWM rectifier-inverter topology for three-phase UPS applications," in *Proc. Eur. Conf. Power Electron. Appl.*, 2007, pp. 1–10.

[11] P. C. Loh, L. Zhang, and F. Gao, "Compact integrated energy systems for distributed generation," *IEEE Trans. Ind. Electron.*, vol. 60, no. 4, pp. 1492–1502, Apr. 2013.

[12] E. C. dos Santos, C. B. Jacobina, and O. I. da Silva, "Six-phase machine drive system with nine-switch converter," in *Proc. 37th Annu. Conf. IEEE Ind. Electron. Soc.*, 2011, pp. 4204–4209.

[13] J. Wei, T. Zhang, L. Shi, and B. Zhou, "Dual-stator doubly salient electromagnetic motor driving system utilizing a nine-switch converter," *IEEE Trans. Ind. Appl.*, vol. 55, no. 2, pp. 1550–1560, Mar./Apr. 2019.

[14] S. Datta, J. P. Mishra, and A. K. Roy, "Unbalance and non-linear stator voltage control of a grid connected DFIG based WECS using NSC," in *Proc. Annu. IEEE India Conf.*, 2015, pp. 1–6.

[15] X. Liu, P. C. Loh, P. Wang, and F. Blaabjerg, "A direct power conversion topology for grid integration of hybrid AC/DC energy resources," *IEEE Trans. Ind. Electron.*, vol. 60, no. 12, pp. 5696–5707, Dec. 2013.

[16] G. Wen, Y. Chen, P. Zhang, and Y. Kang, "Nine-switch-converter-based DFIG wind power system and its dynamic port-current assigned approach for low voltage riding through (LVRT)," in *Proc. IEEE Appl. Power Electron. Conf. Expo.*, 2015, pp. 1324–1330.

[17] A. Kirakosyan, M. S. El Moursi, P. Kanjiya, and V. Khadkikar, "A nine switch converter-based fault ride through topology for wind turbine applications," *IEEE Trans. Power Del.*, vol. 31, no. 4, pp. 1757–1766, Aug. 2016.

[18] H. Gao, B. Wu, and D. Xu, "Nine-switch AC/AC current source converter for microgrid application with model predictive control," *IET Power Electron.*, vol. 10, no. 13, pp. 1759–1766, Oct. 2017.

[19] G. Wen, Y. Chen, Z. Zhong, and Y. Kang, "Dynamic voltage and current assignment strategies of nine-switch-converter-based DFIG wind power system for low-voltage ride-through (LVRT) under symmetrical grid voltage dip," *IEEE Trans. Ind. Appl.*, vol. 52, no. 4, pp. 3422–3434, Jul. 2016.

[20] L Pan, J Zhang, K Wang, B Wang, Y Pang, and L Zhu, "Direct power control without current sensors for nine-switch inverters," *J. Power Electron.*, vol. 18, no. 1, pp. 1–10, Jan. 2018.

[21] D. Zhou and F. Blaabjerg, "Bandwidth oriented proportional-integral controller design for back-to-back power converters in DFIG wind turbine system," *IET Renew. Power Gener.*, vol. 11, no. 7, pp. 941–951, Jun. 2017.

[22] W. Tang, J. Hu, Y. Chang, and F. Liu, "Modeling of DFIG-based wind turbine for power system transient response analysis in rotor speed control timescale," *IEEE Trans. Power Syst.*, vol. 33, no. 6, pp. 6795–6805, Nov. 2018.

[23] G. D. Marques and M. F. Iacchetti, "DFIG topologies for DC networks: A review on control and design features," *IEEE Trans. Power Electron.*, vol. 34, no. 2, pp. 1299–1316, Feb. 2019.

[24] J. Mohammadi, S. Vaez-Zadeh, E. Ebrahimzadeh, and F. Blaabjerg, "Combined control method for grid-side converter of doubly fed induction generator-based wind energy conversion systems," *IET Renewable Power Gener.*, vol. 12, no. 8, pp. 943–952, Nov. 2018.

[25] C. Wu, H. Nian, B. Pang, and P. Cheng, "Adaptive repetitive control of DFIG-DC system considering stator frequency variation," *IEEE Trans. Power Electron.*, vol. 34, no. 4, pp. 3302–3312, Apr. 2019.

[26] S. Yu, T. Fernando, K. Emami, and H. H. Iu, "Dynamic state estimation based control strategy for DFIG wind turbine connected to complex power systems," *IEEE Trans. Power Syst.*, vol. 32, no. 2, pp. 1272–1281, Mar. 2017.

[27] M. Oñate, J. Posada, J. López, J. Quintero, and M. Aredes, "Control of a back-to-back converter as a power transfer system using synchronverter approach," *IET Gener. Transm. Distrib.*, vol. 12, no. 9, pp. 1998–2005, 2018.

[28] Z. Pan, F. Dong, J. Zhao, L. Wang, H. Wang, and Feng, Y, "Combined resonant controller and two-degree-of-freedom PID controller for PMSLM current harmonics suppression," *IEEE Trans. Ind. Electron.*, vol. 65, no. 9, pp. 7558–7568, Sep. 2018.

[29] M. J. Neath, A. K. Swain, U. K. Madawala, and D. J. Thrimawithana, "An optimal PID controller for a bidirectional inductive power transfer system using multiobjective genetic algorithm," *IEEE Trans. Power Electron.*, vol. 29, no. 3, pp. 1523–1531, Mar. 2014.

[30] G. Schoonhoven and M. N. Uddin, "Harmonic injection-based adaptive control of IPMSM motor drive for reduced motor current THD," *IEEE Trans. Ind. Appl.*, vol. 53, no. 1, pp. 483–491, Jan./Feb. 2017.

[31] F. Wang, Y. Wang, Q. Gao, C. Wang, and Y. Liu, "A control strategy for suppressing circulating currents in parallel-connected PMSM drives with individual DC links," *IEEE Trans. Power Electron.*, vol. 31, no. 2, pp. 1680–1691, Feb. 2016.

Kai Wang received the B.S. degree from Tianjin Chengjian University, Tianjin, China, in 2017, where he is currently working toward the master's degree.

His research interests include power converters and motor drives.

Jingmei Zhang received the Ph.D. degrees from Southeast University, Nanjing, China, in 2014.

She is currently a Lecturer with Tianjin Chengjian University, Tianjin, China. Her research interests include nonlinear control and power converters modulation.

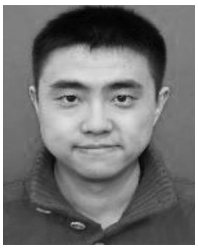

Yi Pang received the Ph.D. degree from Nankai University, Tianjin, China, in 2015.

He is currently a Lecturer with Tianjin Chengjian University, Tianjin, China. His research interests include power converter system and electrical motor drives.

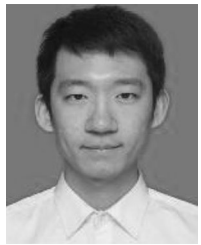

Dongxing Xu received the B.S. degree from Tianjin Chengjian University, Tianjin, China, in 2018, where he is currently working toward the master's degree.

His research interests include power converters and motor drives.

Lei Pan received the Ph.D. degree from the Hebei University of Technology, Tianjin, China, in 2014.

He is currently an Associate Professor with Tianjin Chengjian University, Tianjin, China. His research interests include power converters and motor drives.